• Supplementary File •

BioKG-CMI: a multi-source feature fusion model based on biological knowledge graph for predicting circRNA-miRNA interactions

Mengmeng Wei[1†], Lei Wang[1,5†], Yang Li[4], Zhengwei Li[1,5], Bowei Zhao[3],
Xiaorui Su[3], Yu Wei[6] & Zhuhong You[2]

[1]*School of Computer Science and Technology, China University of Mining and Technology, Xuzhou 221116, China;*
[2]*School of Computer Science, Northwestern Polytechnical University, Xi'an 710129, China;*
[3]*Xinjiang Technical Institute of Physics & Chemistry, Chinese Academy of Sciences, Urumqi 830011, China;*
[4]*School of Computer Science and Information Engineering, Hefei University of Technology, Hefei 230601, China;*
[5]*School of Information Science and Engineering, Zaozhuang University, Zaozhuang 277100, China;*
[6]*School of Information Engineering, Xijing University, Xi'an 710123, China*

Appendix A   Positive and Negative Sample Construction

We primarily employed the CMI-9905 dataset to validate the performance of BioKG-CMI. Constructed by Wang et al. [1], CMI-9905 is sourced from the circBank and circR2Cancer databases [2,3]. Following filtering, 9905 pairs of CMI relationships were obtained, including 2346 circRNAs and 962 miRNAs. Additionally, we also utilized the CMI-9589 dataset to assess the generalization of the model. Originating from the circBank database, CMI-9589 comprises 9589 pairs of CMI relationships with high confidence, including 2115 circRNAs and 821 miRNAs.

An overview of the subcellular localization-based negative sample generation is shown in Figure B1. Specifically, for circRNA, drawing inspiration from RNAlight, we utilize lncLocator to predict the subcellular location of circRNA. On the other hand, for miRNA, we employ miRNALoc to forecast the subcellular location of miRNA [4,5]. Subsequently, samples with different subcellular locations of circRNA and miRNA were used as candidate negative samples. Then, the positive samples among them are deleted to obtain usable negative samples. Finally, we randomly select a subset equal to the number of positive samples from the available negative samples as the negative samples in the experiment.
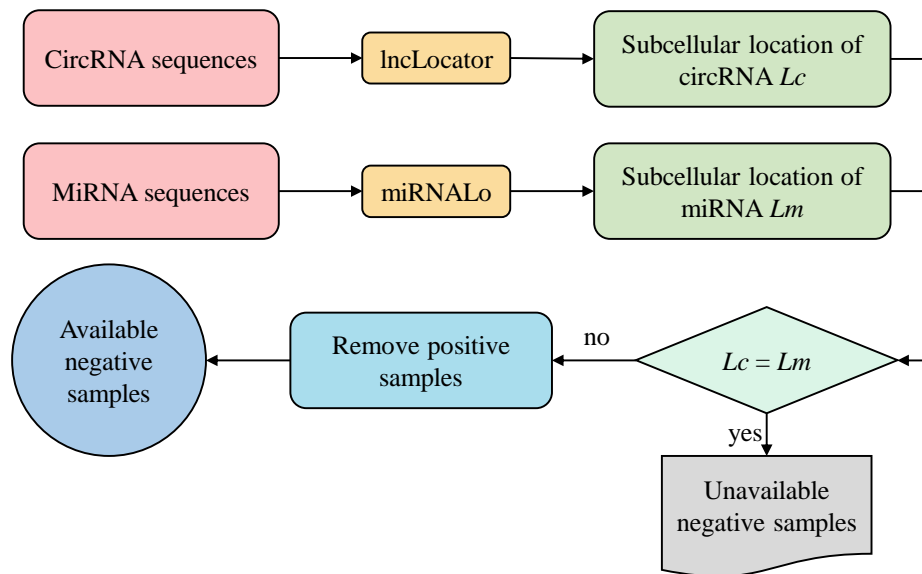

Figure A1   Overview of generating negative samples with subcellular localization.

* Corresponding author (email: leiwang@cumt.edu.cn, zhuhongyou@nwpu.edu.cn)
† Wei M M and Wang L have the same contribution to this work.

Appendix B   BioKG-CMI algorithm

Appendix B.1   Sequence representation learning

Molecular sequences contain rich biological information, and an increasing number of computational methods are being used to mine their features [6]. We utilize natural language processing model BERT for pre-training sequences of circRNA and miRNA [7]. BERT consists of the input layer, encoding layer, and output layer, as illustrated in Figure B1. Firstly, at the input layer, BERT uses the WordPiece algorithm to segment the input sequence and adds [CLS] and [SEP] markers. [CLS] represents the beginning of a statement, and [SEP] serves as a separator mark. The input sequence is divided into Token embeddings, Segment embeddings, and Position embeddings, which respectively represent the semantics of the word, the sentences in which the word is located, and the order relationship within the sentence where the word is located. Then, at the encoding layer, comprising a 12-layer Transformer, embedding vectors are learned bidirectionally based on the self-attention mechanism. Finally, at the output layer, semantic representations for each word, incorporating contextual information, are obtained. The acquired sequence features through this method offer novel possibilities for an in-depth understanding of intricate relationships in biology.
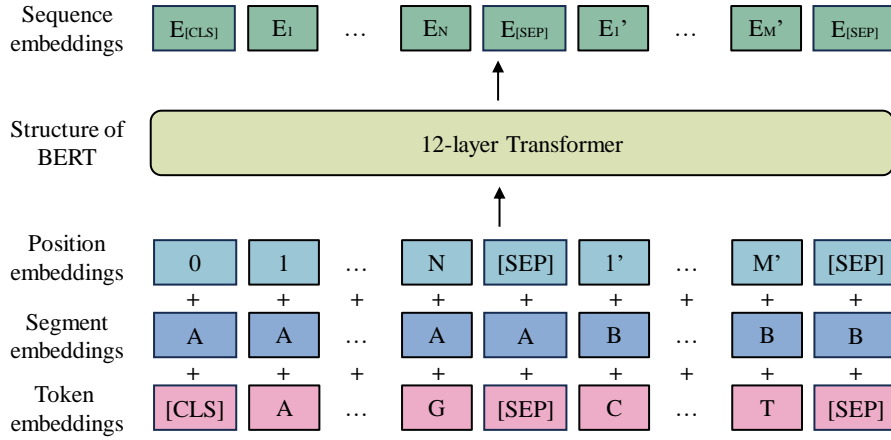

Figure B1   Architecture for pre-training BERT.

Appendix B.2   Spatial proximity calculation

Word Mover's Distance utilizes word2vec in conjunction with Earth Mover's Distance to quantify proximity between sequences [8]. In particular, Word Mover's Distance maps each sequence into word embedding vectors and then quantifies the distances between these word vectors. The logarithmic likelihood calculation formula for the conditional probability between the central word and context word pairs in the sequence is as follows:

$$\frac{1}{T}\sum_{t=1}^{T}\sum_{j\in nb(t)}\log p\left(w_j \mid w_t\right),\tag{B1}$$

where T represents the length of the sequence, w_t denotes the current center word, and $nb(t)$ is the set of neighboring words of word w_t.

To incorporate semantic similarity between words into the document distance metric, the distance l calculation formula between words i and j is as follows:

$$l(i,j) = \|\mathbf{x}_i - \mathbf{x}_j\|_2,\tag{B2}$$

where $\mathbf{x}_i$ represents the embedding of the i-th word in the word2vec mapping space.

The computation of the minimum cumulative cost for the movement of sequence d to sequence d' is as follows:

$$\min_{\mathbf{M}\geqslant 0}\sum_{i,j=1}^{n}\mathbf{M}_{ij}l(i,j),$$
$$\text{s.t.}\quad \sum_{j=1}^{n}\mathbf{M}_{ij}=d_i \quad \forall i\in\{1,\ldots,n\},\tag{B3}$$
$$\sum_{i=1}^{n}\mathbf{M}_{ij}=d_j' \quad \forall j\in\{1,\ldots,n\}.$$

The matrix $\mathbf{M}$ describes the distance between words in two sequences, where each element signifies the distance a word from its respective sequence needs to travel to reach another word in the counterpart sequence. Specifically, $\mathbf{M}$ is a sparse flow matrix, indicating how far word i in sequence d needs to move to reach word j in sequence d'. Additionally, to mitigate computational complexity and filter out noise, we employ PCA to map spatial proximity into a lower-dimensional space representation.

Appendix B.3   Biological knowledge graph representation learning

The introduction of advanced data mining algorithms can extract more complete features [9–12]. In this study, we adopt DisMult to characterize the constructed biological knowledge graph. DisMult utilizes a bilinear mapping function to learn the representation of relationships, which enables the model to embedding-based extraction of logical rules from the knowledge graph [13]. We define a knowledge graph as a triple of "entity-relationship-entity". Each input entity corresponds to a vector, such as e_1 and e_2, and f is the sigmoid function, which is used to convert the input vector and output it. $\mathbf{W}$ represents the initialization projection matrix, and the learned entities are represented as y_{e_1} and y_{e_2}. The calculation is as follows:

$$\mathbf{y}_{e_1} = f\left(\mathbf{W}\mathbf{x}_{e_1}\right), \quad \mathbf{y}_{e_2} = f\left(\mathbf{W}\mathbf{x}_{e_2}\right). \tag{B4}$$

For relational representation learning, we employ a fundamental bilinear function to score the relationship between entities e_1 and e_2. The definition of the bilinear transformation function g_r^b is as follows:

$$g_r^b\left(\mathbf{y}_{e_1}, \mathbf{y}_{e_2}\right) = \mathbf{y}_{e_1}^P \mathbf{A}_r \mathbf{y}_{e_2}, \tag{B5}$$

where P represents the positive sample set. $\mathbf{A}_r$ is the parameter learned during the training process, designed to capture a representation of the specific relationship. Notably, to minimize the number of parameters, the relationship matrix $\mathbf{A}_r$ is constrained to be a diagonal matrix.

To take full advantage of the performance, the Margin Ranking loss function is employed for optimization. It is defined as follows:

$$L(\Omega) = \sum_{(e_1, r, e_2) \in P} \sum_{(e_1', r, e_2') \in P'} \max\left\{ S_{(e_1', r, e_2')} - S_{(e_1, r, e_2)} + 1, 0 \right\}, \tag{B6}$$

where P' represent sets of triplets corresponding to negative samples, respectively. The scoring function for the triplet (e_1, r, e_2), denoted as $S_{(e_1, r, e_2)}$. This loss function aims to ensure that the predicted score for the positive sample is higher than that of the negative sample by a certain margin, which promotes the model to learn graph representations better.

Appendix C   Results

Appendix C.1   Assessment of prediction ability

The results generated by BioKG-CMI on the CMI-9905 using 5-fold CV are shown in Table C1. BioKG-CMI achieved notable performance metrics, with Acc., Prec., Spec., Rec., F1, MCC, AUC, and AUPR reaching 82.19%, 94.81%, 68.23%, 96.14%, 79.23%, 67.15%, 0.9063, and 0.9278, respectively. The ROC curve and PR curve obtained by BioKG-CMI through 5-fold CV on the CMI-9905 data set are shown in Figure C1. In addition, to assess the generalization performance of BioKG-CMI, we conducted a 5-fold CV on the CMI-9589 dataset. Detailed experimental results are presented in Table C2. BioKG-CMI achieved Acc., Prec., Spec., Rec., F1, MCC, AUC, and AUPR of 85.61%, 97.29%, 73.26%, 97.96%, 83.58%, 73.5%, 0.9463, and 0.9581, respectively, on the CMI-9589 dataset.

The ROC curve and PR curve generated through 5-fold CV for BioKG-CMI on the CMI-9589 dataset are depicted in Figure C2. Notably, the standard deviation range in the results of the CMI-9905 dataset is larger than that of the CMI-9589 dataset. These different results may be because the average degree of node connectivity in the CMI-9905 dataset is lower than that in the CMI-9589 dataset.

Table C1   Results of the 5-fold CV for BioKG-CMI on CMI-9905

Test set	Acc. (%)	Prec. (%)	Rec. (%)	Spec. (%)	F1 (%)	MCC (%)	AUC	AUPR
1	83.27	92.24	72.64	93.89	81.28	68.09	0.9098	0.9316
2	83.19	91.96	72.74	93.64	81.23	67.88	0.9004	0.9257
3	83.80	97.92	69.06	98.54	80.99	70.74	0.8977	0.9213
4	80.34	95.39	63.76	96.92	76.43	64.32	0.9291	0.9420
5	80.34	96.52	62.95	97.73	76.20	64.72	0.8944	0.9186
Average	82.19	94.81	68.23	96.14	79.23	67.15	0.9063	0.9278
Std	1.70	2.63	4.70	2.25	2.66	2.66	0.0140	0.0093

Table C2   Results of the 5-fold CV for BioKG-CMI on CMI-9589

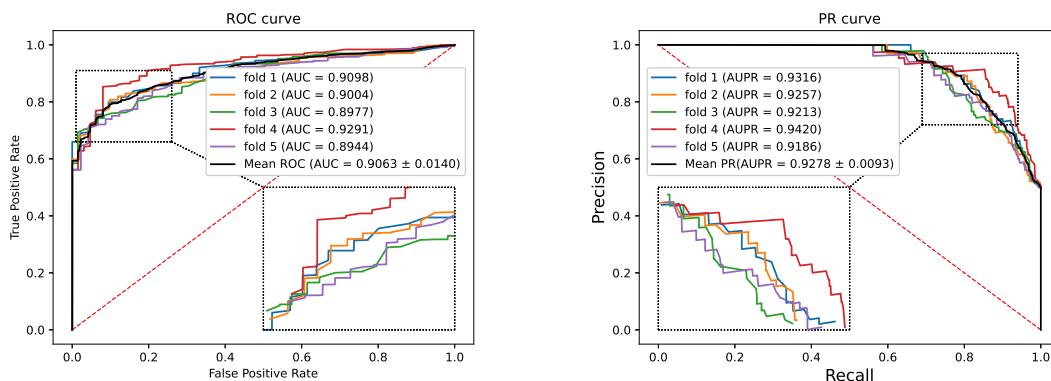| Test set	Acc. (%)	Prec. (%)	Rec. (%)	Spec. (%)	F1 (%)	MCC (%)	AUC	AUPR
1	86.47	98.08	74.40	98.54	84.61	75.16	0.9460	0.9588
2	86.68	97.44	75.34	98.02	84.98	75.32	0.9447	0.9583
3	84.72	97.23	71.48	97.97	82.39	72.02	0.9420	0.9550
4	85.55	98.10	72.52	98.59	83.39	73.66	0.9514	0.9618
5	84.62	95.60	72.56	96.66	82.50	71.33	0.9475	0.9566
Average	85.61	97.29	73.26	97.96	83.58	73.50	0.9463	0.9581
Std	0.96	1.02	1.57	0.78	1.19	1.80	0.0035	0.0025

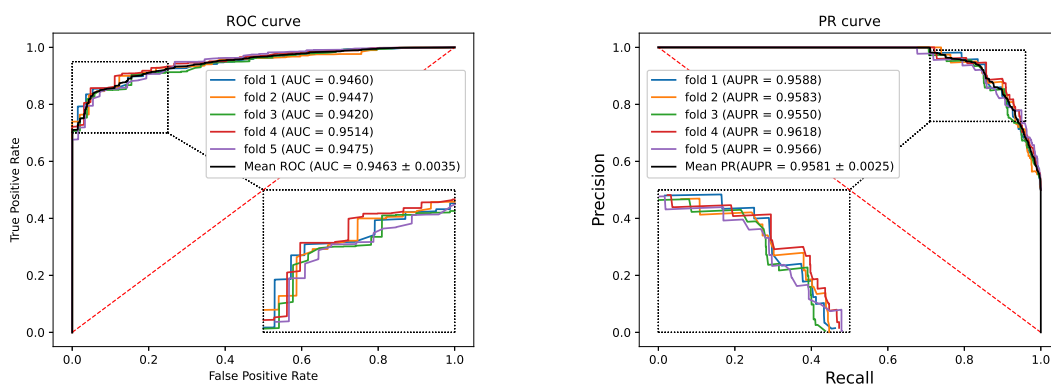**Figure C1** ROC curve and PR curve of BioKG-CMI on CMI-9905.

Figure C2 ROC curve and PR curve of BioKG-CMI on CMI-9589.

Appendix C.2   Comparison of different negative samples

We conducted 5-fold CV experiments on the CMI-9905 dataset, utilizing negative samples generated through subcellular localization and randomly generated negative samples, respectively. Randomly generating negative samples is to pair known circRNAs and miRNAs. Subsequently, after removing the interaction pairs in the known samples, an equal number of samples is randomly selected from the remaining samples to serve as negative samples. The specific comparison results are shown in Figure C3.
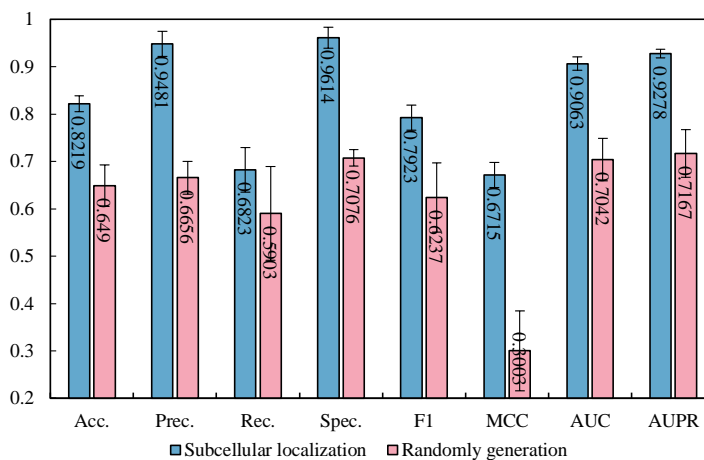

Figure C3 Performance comparison of BioKG-CMI with different negative samples on CMI-9905.

The results show that the predictive performance of negative samples generated by BioKG-CMI through subcellular localization outperforms randomly generated ones. This confirms the effectiveness of employing subcellular localization as a strategy for negative sample generation.

Appendix C.3 Comparison of different feature combinations

The multi-source feature extracted by BioKG-CMI were categorized into three classes: sequence feature, spatial proximity, and knowledge graph feature, marked as SF, SP, and KG. Remove these features in turn to observe the impact on the prediction results. The ablation experiment results of BioKG-CMI on the CMI-9905 dataset using 5-fold CV are shown in Table C3.

Table C3 Ablation experimental of results on CMI-9905

Model	Acc. (%)	Prec. (%)	Rec. (%)	Spec. (%)	F1 (%)	MCC (%)	AUC	AUPR
SF+SP	71.50	77.10	61.10	81.90	68.15	43.96	0.7928	0.8169
SP+KG	78.35	93.89	60.73	95.97	73.62	60.66	0.8897	0.9122
SF+KG	81.08	94.22	66.30	95.85	77.74	65.13	0.9039	0.9251
Ours	**82.19**	**94.81**	**68.23**	**96.14**	**79.23**	**67.15**	**0.9063**	**0.9278**

The results show that the model's predictive performance, which fuses multi-source feature, achieved optimal results. On the other hand, the model that excluded the knowledge graph feature exhibited the poorest performance, followed by the model without the sequence feature. This indicates that effectively integrating of multi-source feature is crucial for improving model performance, with knowledge graph features playing a key role in feature fusion.

Appendix C.4 Comparison with other graph representation methods

We compared DisMult with SDNE [14], DeepWalk [15], and LINE [16], while keeping other parts of BioKG-CMI unchanged. The objective prediction results of 5-fold CV experiments using different graph representation methods are shown in Figure C4, where the width of the line represents the standard deviation. The findings indicate that the neural learning-based bilinear model, DisMult, outperforms the performance of three other methods.
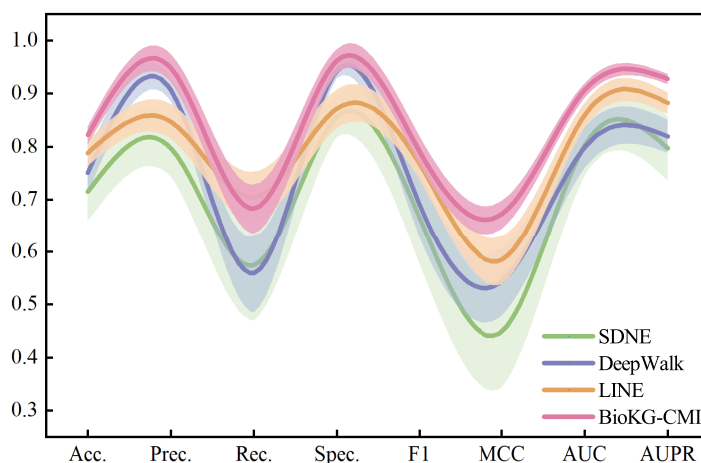

Figure C4 Performance comparison of BioKG-CMI using different graph representation learning methods on CMI-9905.

Embedding dimension is a crucial parameter in graph representation learning methods, which can directly affect the expressive ability of the learned features. A lower embedding dimension may result in information loss, hindering the model's ability to capture the intricate structure information of the graph fully. Conversely, a higher embedding dimension may give rise to the curse of dimensionality, increasing computational costs and making the model more prone to overfitting. Therefore, we systematically examine the impact of knowledge graph features at different dimensions on performance, including 32, 64, 128, 256, and 512. The experimental results of comparing different embedding dimensions on the CMI-9905 dataset are shown in Table C4. The AUC values under embedding dimensions 32, 64, 128, 256, and 512 are 0.8501, 0.8857, 0.9063, 0.8510, and 0.9019, respectively.

Table C4 Results of different embedding dimensions on CMI-9905

Dimensions	Acc. (%)	Prec. (%)	Rec. (%)	Spec. (%)	F1 (%)	MCC (%)	AUC	AUPR
32	78.21	91.23	62.44	93.98	74.12	59.47	0.8501	0.8777
64	81.20	89.47	**70.87**	91.52	78.99	63.88	0.8857	0.9053
128	**82.19**	**94.81**	68.23	**96.14**	**79.23**	**67.15**	**0.9063**	**0.9278**
256	76.17	79.94	69.94	82.39	74.58	52.78	0.8510	0.8785
512	81.68	91.62	69.69	93.66	79.08	65.29	0.9019	0.9164

Appendix C.5 Comparison of different classifiers

We used the Gradient Boosting Decision Tree (GBDT) [17], Logistic Regression (LR), Random Forest (RF), and AdaBoost classifier for prediction, respectively. The results of 5-fold CV experiments on the CMI-9905 dataset using different classifiers are presented in Table C5. Additionally, we have plotted the mean ROC curve, as illustrated in Figure C5.

The AUC values of GBDT, LR, RF, and AdaBoost are 0.8887, 0.854, 0.8913, and 0.9063, respectively. This suggests that the choice of AdaBoost classifier is reasonable, as its robust classification and predictive capabilities provide strong support for accurately predicting CMI.

Table C5   Results of different classifiers on CMI-9905

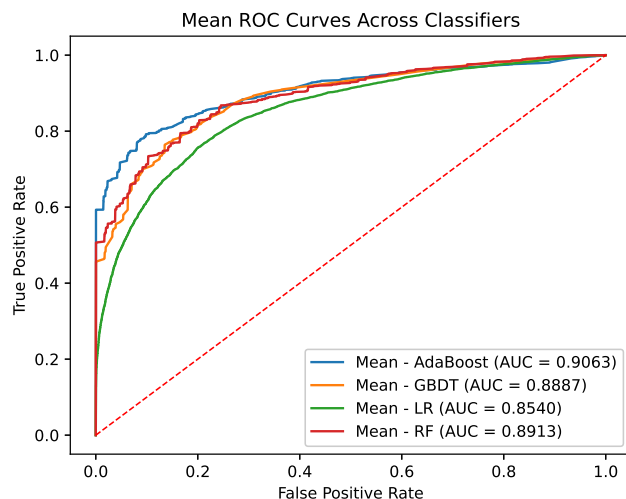| Classifier	Acc. (%)	Prec. (%)	Rec. (%)	Spec. (%)	F1 (%)	MCC (%)	AUC	AUPR
GBDT	79.96	89.84	67.62	92.30	76.95	61.95	0.8887	0.8940
LR	78.04	79.74	**75.17**	80.90	77.37	56.19	0.8540	0.8655
RF	79.87	84.93	72.77	86.97	78.28	60.47	0.8913	0.9093
AdaBoost	**82.19**	**94.81**	68.23	**96.14**	**79.23**	**67.15**	**0.9063**	**0.9278**

Figure C5   Mean ROC curves of BioKG-CMI using different classifiers on CMI-9905.

Appendix C.6   Comparison with other cutting-edge methods

The comparison results on the CMI-9905 dataset are presented in Table C6, where the AUC values of KGDCMI [18], WSCD [19], SGCNCMI [20], JSNDCMI [1], KS-CMI [21], and BioKG-CMI are 0.893, 0.8923, 0.8942, 0.9003, 0.9086 and 0.9063 respectively. The comparison results on the CMI-9589 dataset are shown in Table C7, with AUC values for CMIVGSD [22], SGCNCMI, KGD-CMI, GCNCMI [23], BioDGW-CMI [24], and BioKG-CMI being 0.8804, 0.9015, 0.9041, 0.9320, 0.9179, and 0.9463, respectively. Additionally, the p-values of AUC on CMI-9905 and CMI-9589 are 0.0092 and 0.0106, both less than 0.05. These results further indicate that BioKG-CMI exhibits significant differences compared to other models.

Table C6   Comparison results with cutting-edge methods on CMI-9905

Model	KGDCMI	WSCD	SGCNCMI	JSNDCMI	BioDGW-CMI	BioKG-CMI
AUC	0.8930	0.8923	0.8942	0.9003	0.9026	**0.9063**
AUPR	0.8767	0.8935	0.8887	0.8999	0.8962	**0.9278**

Table C7   Comparison results with cutting-edge methods on CMI-9589

Model	CMIVGSD	SGCNCMI	KGDCMI	GCNCMI	KS-CMI	BioKG-CMI
AUC	0.8804	0.9015	0.9041	0.9320	0.9179	**0.9463**
AUPR	0.8629	0.9011	0.8937	0.9396	0.9181	**0.9581**

Appendix C.7   Case studies

Annually, over 12,500 individuals in the United States receive a diagnosis of laryngeal cancer, with laryngeal squamous cell carcinoma (LSCC) constituting 90% of all malignant tumors in the larynx [25, 26]. Research indicates that ncRNA can influence LSCC cells through miRNA sponging [27]. Glioblastoma (GBM) is a tumor type caused by astrocytes, a type of glial cell [28]. GBM tumor cells are composed of various cells that multiply rapidly in the body, making them difficult to treat. Gastric cancer ranks second in cancer mortality rates, and a growing body of evidence suggests that the aberrant expression of miRNA may present novel therapeutic

Table C8   The top 10 circRNAs and miRNAs associated with cancers

Rank	CircRNA	MiRNA	Evidence (PMID)
1	hsa_circ_0044520	hsa-miR-4726-5p	30282067
2	hsa_circ_0023303	hsa-miR-646	31951319
3	hsa_circ_0092012	miR-486-3p	31384171
4	hsa_circ_0081119	hsa-miR-4726-5p	Unconfirmed
6	hsa_circ_0043949	hsa-miR-5195-3p	31823158
4	hsa_circ_0043949	hsa-miR-1257	31823158
5	hsa_circ_0043949	hsa-miR-140-3p	Unconfirmed
6	hsa_circ_0000376	hsa-miR-375	31307199
7	hsa_circ_0008365	hsa-miR-375	31199037
8	hsa_circ_0004928	hsa-miR-375	31307199
9	hsa_circ_0044520	hsa-miR-4726-5p	30282067
10	hsa_circ_0023303	hsa-miR-646	31951319

opportunities [29, 30]. The top 10 circRNA-miRNA relationships associated with these three types of cancer are presented in Table C8, with eight pairs validated and evidence provided.

For instance, hsa_circ_0044520 exhibits a significant upregulation in LSCC. It plays a crucial regulatory role by acting as a sponge for hsa-miR-4726-5p [31]. Resistance of temozolomide (TMZ) limits its efficacy in GBM. The hsa_circ_0043949 regulates TMZ resistance by acting as a sponge for hsa-miR-876-3p and provides a potential therapeutic target for GBM treatment [32]. The hsa_circ_0008365 suppresses solid tumor growth by upregulating the expression of has-miR-375, potentially offering novel insights into the treatment of GC [33].

References

1 Wang X F, Yu C Q, You Z H, et al. A feature extraction method based on noise reduction for circRNA-miRNA interaction prediction combining multi-structure features in the association networks. Briefings in Bioinformatics, 2023, 24(3): bbad111.

2 Liu M, Wang Q, Shen J, et al. Circbank: a comprehensive database for circRNA with standard nomenclature. RNA biology, 2019, 16(7): 899-905.

3 Lan W, Zhu M, Chen Q, et al. CircR2Cancer: a manually curated database of associations between circRNAs and cancers. Database, 2020, 2020: baaa085.

4 Cao Z, Pan X, Yang Y, et al. The lncLocator: a subcellular localization predictor for long non-coding RNAs based on a stacked ensemble classifier. Bioinformatics, 2018, 34(13): 2185-2194.

5 Meher P K, Satpathy S, Rao A R. miRNALoc: predicting miRNA subcellular localizations based on principal component scores of physico-chemical properties and pseudo compositions of di-nucleotides. Scientific Reports, 2020, 10(1): 14557.

6 Luo X, Wu H, Li Z. NeuLFT: A novel approach to nonlinear canonical polyadic decomposition on high-dimensional incomplete tensors. IEEE Transactions on Knowledge and Data Engineering, 2022.

7 Devlin J, Chang M W, Lee K, et al. Bert: Pre-training of deep bidirectional transformers for language understanding. arXiv preprint arXiv:1810.04805, 2018.

8 Kusner M, Sun Y, Kolkin N, et al. From word embeddings to document distances. In: International conference on machine learning. PMLR, 2015: 957-966.

9 Bi F, He T, Xie Y, et al. Two-stream graph convolutional network-incorporated latent feature analysis. IEEE Transactions on Services Computing, 2023.

10 Luo X, Yuan Y, Chen S, et al. Position-transitional particle swarm optimization-incorporated latent factor analysis. IEEE Transactions on Knowledge and Data Engineering, 2020, 34(8): 3958-3970.

11 Luo X, Zhong Y, Wang Z, et al. An alternating-direction-method of multipliers-incorporated approach to symmetric non-negative latent factor analysis. IEEE Transactions on Neural Networks and Learning Systems, 2021, 34(8): 4826-4840.

12 Zhou H, He T, Ong Y S, et al. Differentiable Clustering for Graph Attention. IEEE Transactions on Knowledge and Data Engineering, 2024.

13 Yang B, Yih W, He X, et al. Embedding entities and relations for learning and inference in knowledge bases. arXiv preprint arXiv:1412.6575, 2014.

14 Wang D, Cui P, Zhu W. Structural deep network embedding. In: Proceedings of the 22nd ACM SIGKDD international conference on Knowledge discovery and data mining. 2016: 1225-1234.

15 Perozzi B, Al-Rfou R, Skiena S. Deepwalk: Online learning of social representations. In: Proceedings of the 20th ACM SIGKDD international conference on Knowledge discovery and data mining. 2014: 701-710.

16 Tang J, Qu M, Wang M, et al. Line: Large-scale information network embedding. In: Proceedings of the 24th international conference on world wide web. 2015: 1067-1077.

17 Friedman J H. Greedy function approximation: a gradient boosting machine. Annals of statistics, 2001: 1189-1232.

18 Wang X F, Yu C Q, Li L P, et al. KGDCMI: a new approach for predicting circRNA–miRNA interactions from multi-source information extraction and deep learning. Frontiers in Genetics, 2022, 13: 958096.

19 Guo L X, You Z H, Wang L, et al. A novel circRNA-miRNA association prediction model based on structural deep neural network embedding. Briefings in Bioinformatics, 2022, 23(5): bbac391.

20 Yu C Q, Wang X F, Li L P, et al. SGCNCMI: a new model combining multi-modal information to predict circRNA-related miRNAs, diseases and genes. Biology, 2022, 11(9): 1350.

21 Wang X F, Yu C Q, You Z H, et al. KS-CMI: A circRNA-miRNA interaction prediction method based on the signed graph neural network and denoising autoencoder. Iscience, 2023, 26(8).

22 Qian Y, Zheng J, Zhang Z, et al. CMIVGSD: circRNA-miRNA interaction prediction based on Variational graph auto-encoder and singular value decomposition. In: 2021 IEEE International Conference on Bioinformatics and Biomedicine (BIBM). IEEE, 2021: 205-210.

23 He J, Xiao P, Chen C, et al. GCNCMI: a graph convolutional neural network approach for predicting circRNA-miRNA

interactions. Frontiers in Genetics, 2022, 13: 959701.

24 Wang X F, Yu C Q, You Z H, et al. An efficient circRNA-miRNA interaction prediction model by combining biological text mining and wavelet diffusion-based sparse network structure embedding. Computers in Biology and Medicine, 2023, 165: 107421.

25 Young R J, Urban D, Angel C, et al. Frequency and prognostic significance of p16INK4A protein overexpression and transcriptionally active human papillomavirus infection in laryngeal squamous cell carcinoma. British journal of cancer, 2015, 112(6): 1098-1104.

26 Li P, Lin X J, Yang Y, et al. Reciprocal regulation of miR-1205 and E2F1 modulates progression of laryngeal squamous cell carcinoma. Cell Death & Disease, 2019, 10(12): 916.

27 Li X, Xu F, Meng Q, et al. Long noncoding RNA DLEU2 predicts a poor prognosis and enhances malignant properties in laryngeal squamous cell carcinoma through the miR-30c-5p/PIK3CD/Akt axis. Cell death & disease, 2020, 11(6): 472.

28 Saadatpour L, Fadaee E, Fadaei S, et al. Glioblastoma: exosome and microRNA as novel diagnosis biomarkers. Cancer gene therapy, 2016, 23(12): 415-418.

29 Xu Y, Zhao F, Wang Z, et al. MicroRNA-335 acts as a metastasis suppressor in gastric cancer by targeting Bcl-w and specificity protein 1. Oncogene, 2012, 31(11): 1398-1407.

30 Ding L, Xu Y, Zhang W, et al. MiR-375 frequently downregulated in gastric cancer inhibits cell proliferation by targeting JAK2. Cell research, 2010, 20(7): 784-793.

31 Fan Y, Xia X, Zhu Y, et al. Circular RNA expression profile in laryngeal squamous cell carcinoma revealed by microarray. Cellular Physiology and Biochemistry, 2018, 50(1): 342-352.

32 Li X, Wang N, Leng H, et al. Hsa_circ_0043949 reinforces temozolomide resistance via upregulating oncogene ITGA1 axis in glioblastoma. Metabolic brain disease, 2022, 37(8): 2979-2993.

33 Liu J, Song S, Lin S, et al. Circ-SERPINE2 promotes the development of gastric carcinoma by sponging miR-375 and modulating YWHAZ. Cell proliferation, 2019, 52(4): e12648.